

Bridging Quantum Computing and Nuclear Structure: Atomic Nuclei on a Trapped-Ion Quantum Computer

Sota Yoshida,^{1,2,*} Takeshi Sato,^{3,4,5} Takumi Ogata,³ and Masaaki Kimura^{2,6}

¹*School of Data Science and Management, Utsunomiya University, Mine, Utsunomiya, 321-8505, Japan*

²*RIKEN Nishina Center for Accelerator-based Science, RIKEN, Wako 351-0198, Japan*

³*Graduate School of Engineering, The University of Tokyo,
7-3-1 Hongo, Bunkyo-ku, Tokyo 113-8656, Japan*

⁴*Photon Science Center, School of Engineering, The University of Tokyo,
7-3-1 Hongo, Bunkyo-ku, Tokyo 113-8656, Japan*

⁵*Research Institute for Photon Science and Laser Technology,
The University of Tokyo, 7-3-1 Hongo, Bunkyo-ku, Tokyo 113-0033, Japan*

⁶*Department of Physics / Quark Nuclear Science Institute,
Graduate School of Science, The University of Tokyo,
7-3-1 Hongo, Bunkyo-ku, Tokyo 113-0033, Japan*

We demonstrate quantum simulations of strongly correlated nuclear many-body systems on the RIKEN-Quantinuum Reimei trapped-ion quantum computer, targeting ground states of oxygen, calcium, and nickel isotopes. By combining a hard-core-boson representation of the nuclear shell model with a pair-unitary coupled-cluster doubles ansatz, we achieve sub-percent relative error in the ground-state energies compared to noise-free statevector simulations. Our approach leverages symmetry-aware state preparation and particle-number post-selection to efficiently capture pairing correlations characteristic of systems with same-species nucleons. These findings highlight the viability of high-fidelity trapped-ion platforms for nuclear physics applications and provide a foundation for scaling to more complex nuclear systems.

I. INTRODUCTION

Quantum simulation of many-body systems is a leading application of quantum computing, with potential impact across quantum chemistry, condensed-matter physics, nuclear physics and so on. While quantum algorithms and hardware have advanced rapidly, demonstrating clear advantage for interacting many-body problems remains an open challenge. For example, a recent study [1] identified scenarios in which quantum devices can outperform classical algorithms for certain spin models. Nonetheless, general claims of quantum advantage for many-body systems remain inconclusive and require careful, system-specific analysis.

On near-term devices, variational approaches such as the Variational Quantum Eigensolver [2, 3] rely crucially on the choice of an ansatz that balances implementability and expressivity. Common families of ansätze — including unitary coupled cluster (UCC) variants — can be effective in some domains but often suffer from optimization difficulties, called barren plateaus [4], or unfavorable scaling of parameters and gate depth as system size grows. This situation has evoked a broader consideration of quantum algorithms beyond NISQ towards fault-tolerant quantum computing (FTQC), leading to a term like Early Fault-Tolerant Quantum Computing (E-FTQC) [5]. In such situations, it is essential to broadly examine each component of quantum computation—namely, state preparation (also simply called the

ansatz), quantum algorithms, and measurement strategies for evaluating the observable of interest—for each specific problem.

The first part, the choice of the ansatz, is particularly crucial. This is because the success of most of quantum algorithms for quantum many-body problems largely depends on the quality of the prepared quantum state, i.e., the overlap between the prepared state and the target state. In spin systems or chemical systems, various ansätze have been proposed, such as UCC-family, and ones based on matrix product states or tensor network states more generally [6–8]. Compared to other areas tackling quantum many-body problems, nuclear physics studies have seen relatively limited applications of quantum computing, despite several pioneering works [9–11], and recent reviews [12, 13]. To date, only a few ansätze have been explored for nuclear systems, almost exclusively based on the unitary coupled cluster (UCC) family [11, 14, 15] with some variations such as Adapt-VQE [16]. A seminal work investigated the applicability of the UCC + Adapt-VQE to the nuclear shell model [11], where the number of CNOT gates required to achieve a given accuracy for shell-model calculations of oxygen and calcium isotopes was estimated.

Nuclear many-body systems are distinguished from other quantum many-body systems by exceptionally strong correlations arising from the nature of nuclear forces, posing a unique challenge for both classical and quantum computing. Even in the low-energy regime, where nucleons are the only explicit baryonic degrees of freedom, the problem is complicated by the fact that protons and neutrons—fermions of nearly equal mass—interact through multiple channels in an intricate man-

* syoshida@a.utsunomiya-u.ac.jp

ner. This results in a large number of non-negligible Hamiltonian terms and strong non-locality. Furthermore, anisotropic components of the interaction, such as tensor forces [17] and three-body forces [18], play an essential role in describing the rich phenomena of nuclear systems. These features are generally difficult to capture with a simple wave-function ansatz. Another manifestation of the complexity is entanglement entropy, which in nuclear systems obeys a volume law rather than an area law [19], hindering straightforward application of tensor networks.

Consequently, most quantum-computing studies of nuclear structure have focused on small systems or relied on classical simulators. Reported errors in ground-state energy estimates on quantum hardware range from 4 – 13% for ${}^6\text{Li}$ [14] and 3 – 13% for oxygen isotopes [15]. In our previous work [20], we achieved relative errors below 0.1% for ${}^6\text{He}$ and ${}^{18}\text{O}$, and about 1% for ${}^{42}\text{Ca}$ on an IBM superconducting quantum device. However, the target systems were limited to valence two-neutron configurations and our method is not straightforwardly extendable to more general nuclear systems. This motivates the present work to develop more general and scalable approaches.

In this work, we introduce a hard-core-boson (HCB) mapping of the nuclear shell model combined with the pair-unitary coupled-cluster doubles (pUCCD) ansatz, which efficiently captures strong pairing correlations between nucleons of the same species. While pUCCD ansatzes have been shown to be effective for chemical systems [21–23], this study reports, to our knowledge, the first demonstration of pUCCD applied to nuclear many-body systems on a quantum device. Implemented on the high-fidelity trapped-ion processor RIKEN-Quantum Reimei, and augmented by symmetry-aware ansatzes and post-selection techniques, our approach yields ground-state energies for oxygen, calcium, and nickel isotopes that agree with noise-free statevector simulations within sub-percent relative error. These results establish a new experimental benchmark for quantum simulations of strongly correlated nuclear systems and demonstrate the near-term potential of trapped-ion platforms for nuclear-structure calculations.

This paper is organized as follows. In Sec. II, we describe the methods used in this work, including the Hamiltonian mapping, the adopted ansatz, and the measurement strategies. In Sec. III, we present the results for oxygen, calcium, and nickel isotopes, noise-free simulations and hardware experiments. Finally, we summarize our findings and discuss future outlooks in Sec. IV.

II. METHODS

A. Target systems and Hamiltonian mapping

General Shell-model Hamiltonians with up to two-body interactions can be expressed as

$$\hat{H} = \sum_i h_{ij} a_i^\dagger a_j + \frac{1}{4} \sum_{ijkl} V_{ijkl} a_i^\dagger a_j^\dagger a_l a_k, \quad (1)$$

where i denotes the single-particle state characterized by the quantum numbers $\{n, l, j, j_z, t_z\}$. Here, n is the principal quantum number, l the orbital angular momentum, j the total angular momentum, j_z its projection of j onto the z -axis, and t_z the isospin projection.

For systems within single major shell, as in this work, the one-body term reduces to the diagonal form $\varepsilon_i \equiv h_{ii}$, called the single-particle energies (SPEs). The fermionic creation and annihilation operators, a_i^\dagger and a_i , act on these single-particle states, while V_{ijkl} denotes the two-body matrix elements (TBMEs).

These SPEs and TBMEs can be either derived from the realistic nucleon-nucleon interactions or from the phenomenological adjustments to reproduce experimental data for binding energies, excitation energies, and so on. The target nuclei, model space and adopted interactions in this work are summarized in Table I. The methods in this work can be applied to any other interactions including microscopically derived ones as far as one considers similar systems with same-species nucleons under the methods described below. Diagonalization with these interactions can be reproduced using publicly available codes such as KSHELL [24] or NuclearToolkit.jl [25].

Once the Hamiltonian is defined, one can diagonalize the Hamiltonian in a given model space by means of variants of Configuration Interaction (CI) methods, known as the nuclear shell model in nuclear physics community. In this work, full configuration interaction (FCI) refers to exact diagonalization within the selected valence space, following the convention of quantum chemistry (rather than the no-core shell model definition often used in nuclear physics).

A useful truncation of CI is the doubly occupied configuration interaction (DOCI) method, equivalent to restricting the shell-model space to zero-seniority configurations, i.e., considering only time-reversed nucleon pairs as active degrees of freedom. In even-neutron systems, DOCI often provides a good approximation to FCI and is exact for two-valence-neutron $J = 0$ states. This DOCI method has been also used in nuclear physics and proven

TABLE I. Target nuclei, interactions, and model spaces.

Nuclide	Interaction	Model space
${}^{18-26}\text{O}$	USDB [26]	sd ($1s_{1/2}, 0d_{3/2}, 0d_{5/2}$)
${}^{42-58}\text{Ca}$	GXPf1A [27]	pf ($1p_{1/2}, 1p_{3/2}, 0f_{5/2}, 0f_{7/2}$)
${}^{58-76}\text{Ni}$	JUN45 [28]	$jj45$ ($1p_{1/2}, 1p_{3/2}, 0f_{5/2}, 0g_{9/2}$)

to be a good approximation to even-number neutron systems [29]. Thus, DOCI serves as an important benchmark in this work.

Another viable method for approximating FCI and/or DOCI is the use of pair coupled cluster methods and their extensions [21–23, 30–32]. Whereas the methods have been successfully applied to pairing Hamiltonians (also known as BCS Hamiltonians) in the nuclear physics context, their applications to more general shell-model Hamiltonians remain limited and warrant further exploration.

In the case of electronic structure calculations, the natural assumption on the *pair* degree of freedom is to consider the spin up and spin down electrons as a pair. Detailed derivations of such zero-seniority Hamiltonian for electronic structure calculations can be found in e.g. [31]. For nuclear many-body methods one has more freedom involved in the system, so one can consider the pairs of nucleons with different spins and/or different orbitals. For this reason, we will detail the way to introduce the paired form of a nuclear shell-model Hamiltonian.

The hard-core-boson (HCB) representation provides a natural way to introduce paired degrees of freedom by folding each time-reversed single-particle pair (i, \bar{i}) into a single boson-like site that can be occupied or empty but forbids multiple occupancy. Figure 1 illustrates this mapping for ^{22}O on top of the ^{16}O inert core: the valence single-particle states are grouped into pair orbitals, which reduces the number of active degrees of freedom (and hence qubits). The single-particle states in the original fermionic representation are specified by the quantum numbers $\{n, l, j, j_z, t_z\}$, leading to 12 single-particle states for both protons and neutrons in the *sd* shell. In the HCB representation, these 12 single-particle states form 6 pair orbitals for neutrons, each represented by a qubit. Focusing on even-number neutron systems and terms involving time-reversed pairs, the shell-model Hamiltonian can be expressed as

$$H = \sum_{i<0} \varepsilon_i (a_i^\dagger a_i + a_{\bar{i}}^\dagger a_{\bar{i}}) + \sum_{i<0} V_{i\bar{i}i\bar{i}} a_i^\dagger a_{\bar{i}}^\dagger a_{\bar{i}} a_i + \sum_{i \neq j < 0} V_{i\bar{i}j\bar{j}} a_i^\dagger a_{\bar{i}}^\dagger a_j a_{\bar{j}} + \frac{1}{4} \sum_{i,j \notin \{i,\bar{i}\}} V_{ijij} n_i n_j, \quad (2)$$

where $i < 0$ denotes single-particle states with negative j_z values, and \bar{i} is the time-reversal partner of the single-particle state i . The last term, absent in the valence two-neutron systems studied previously [20], can be regarded as a mean-field contribution from other occupied pairs. Then, the Hamiltonian can be expressed in terms of the paired operators defined below:

$$A_i^\dagger = a_i^\dagger a_{\bar{i}}^\dagger, \quad (3)$$

$$A_{\bar{i}} = a_{\bar{i}} a_i, \quad (4)$$

$$N_{\bar{i}} = \frac{1}{2} (n_i + n_{\bar{i}}) = \frac{1}{2} (a_i^\dagger a_i + a_{\bar{i}}^\dagger a_{\bar{i}}), \quad (5)$$

where A_i^\dagger and $A_{\bar{i}}$ are the pair creation and annihilation

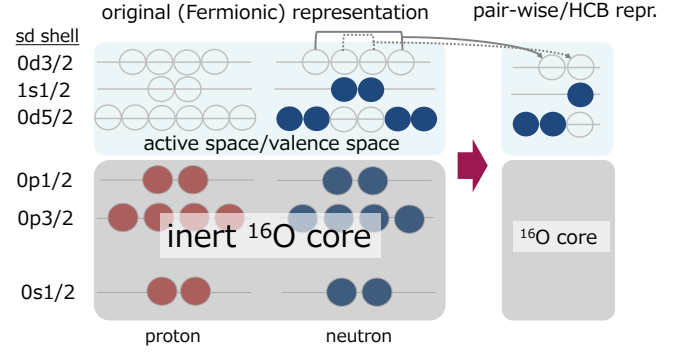


FIG. 1. Schematics of the hard-core boson (HCB) representation. This example shows a configuration of ^{22}O nucleus on top of the inert core ^{16}O . The active (valence) space consists of $1s_{1/2}$, $0d_{3/2}$, and $0d_{5/2}$ single-particle states.

operators, and $N_{\bar{i}}$ is the pair occupation number operator, \bar{i} denotes the pair index corresponding to the single-particle states i and \bar{i} . Then, the Hamiltonian in Eq. (2) can be rewritten as

$$H_{\text{HCB}} = \sum_{\bar{i}} (\varepsilon_{\bar{i}} + V_{\bar{i}\bar{i}}^p) N_{\bar{i}} + \sum_{i \neq j} V_{ij}^p A_i^\dagger A_j + \sum_{i \neq j} V_{ij}^m N_{\bar{i}} N_{\bar{j}}, \quad (6)$$

$$\varepsilon_{\bar{i}} \equiv 2\varepsilon_i = \varepsilon_i + \varepsilon_{\bar{i}}, \quad (7)$$

$$V_{ij}^p \equiv V_{i\bar{i}j\bar{j}}, \quad (8)$$

$$V_{ij}^m \equiv V_{ijij} + V_{i\bar{j}i\bar{j}} + V_{i\bar{j}\bar{j}i} + V_{i\bar{j}\bar{i}j}, \quad (9)$$

where V^p and V^m are introduced to emphasize the pairing and monopole nature of the interactions, respectively. The factor $1/2$ in Eq. (5) is sometimes omitted (as in our earlier work [20]), but is retained here to interpret $N_{\bar{i}}$ as the occupation number of a pair degree of freedom. More details on this derivation are provided in the Supplemental Material [33].

The paired-neutron operators satisfy bosonic commutation relations, as detailed in e.g. [20, 21, 31], but multiple occupancy of the same pair is forbidden, leading to the term hard-core boson. A key advantage of the HCB representation—beyond the qubit reduction—is the elimination of non-locality. From Jordan-Wigner mappings, Pauli-Z terms appear to maintain the anti-commutation relations of the fermionic operators. In some literature, these Pauli-Z terms are omitted on purpose, which is referred to as qubit excitation in Refs. [34, 35], as a hardware-efficient mapping. However, in the HCB representation, those Pauli-Z terms naturally cancel out. Hence, one can map the Hamiltonian to the Pauli op-

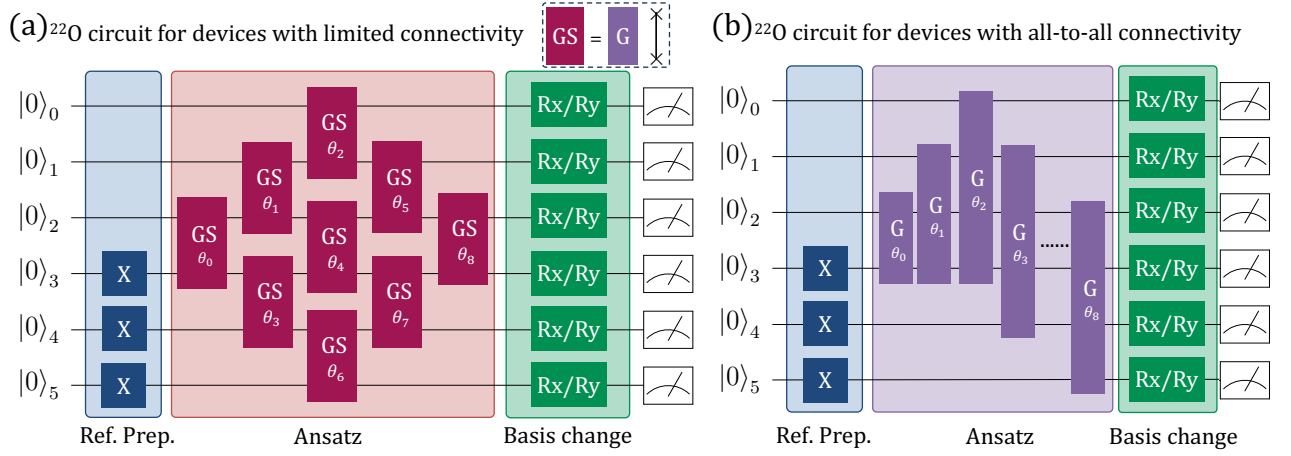


FIG. 2. Sketched quantum circuits for preparing the pUCCD ansatz taking ^{22}O as an example. Original single-particle states in the sd shell consist of twelve states for neutrons, which are now represented by six qubits in the HCB representation. (a) Circuit layout suitable for devices with heavy-hexagon connectivity. (b) Circuit layout for all-to-all connectivity. First, the reference state is prepared by applying X gates to qubits. Then, Givens rotations are applied to take into account particle-hole excitations of nucleon pairs. Single-qubit rotations are applied as needed prior to measuring Hamiltonian expectation values.

erators into simple forms as

$$H_{\text{HCB;q}} = \sum_i \frac{\varepsilon_i + V_{ii}}{2} (I_i - Z_i) + \frac{1}{4} \sum_{i \neq j} V_{ij} (X_i X_j + Y_i Y_j) + \frac{1}{4} \sum_{i \neq j} V_{ij}^m (I_i - Z_i)(I_j - Z_j), \quad (10)$$

where i denotes the pair index of single-particle states in the valence space specified by n (principal quantum number), l (orbital angular momentum), j (total angular momentum), $|j_z|$ (absolute value of the angular momentum projection on the z -axis), and t_z (isospin projection) quanta.

All terms of the Hamiltonian Eq. (10) except the second are diagonal in the computational basis and can be measured directly by measuring the expectation values of the Pauli- Z operators. One needs additional circuits to measure the non-diagonal terms $XX + YY$, which will be discussed later in Sec. II C.

B. ansatze

The ansatz, circuit for state preparation, plays a central role in quantum algorithms both in the NISQ and FTQC regimes. In practice, the ansatz must satisfy two requirements: (1) it should be implementable on available quantum hardware, and (2) it should be expressive enough to approximate, e.g., the true ground state with high fidelity.

In this work, we employ the pair unitary coupled cluster doubles (pUCCD) ansatz for even-even multi-neutron systems within the HCB representation. The pUCCD ansatz is a quantum version of the pair coupled cluster doubles method. A seminal work on the pUCCD ansatz

in the context of quantum computing is found in Ref. [21], where strategies for measurement and post-selection were also proposed. In chemistry, pUCCD has been successfully applied to systems of paired electrons with spin up and spin down [21–23]. For nuclear systems, the pUCCD ansatz has not been explored previously (to our knowledge), and our work represents the first application of this approach to nuclear structure calculations.

The pUCCD ansatz is expressed as

$$|\psi_{\text{pUCCD}}\rangle = \exp(T - T^\dagger) |\text{ref.}\rangle \equiv U |\text{ref.}\rangle, \quad (11)$$

where T is the cluster operator and $|\text{ref.}\rangle$ is a reference state. For paired-neutron excitations, the unitary operator takes the form

$$U = \exp \left[\sum_{ph} t_h^p (A_p^\dagger A_h - A_h^\dagger A_p) \right], \quad (12)$$

with t_h^p the cluster amplitudes, and A_p^\dagger, A_h the pair creation and annihilation operators, Eqs. (3) and (4), respectively. The indices p and h denote the particle and hole states, respectively. Mapping to Pauli operators yields

$$U_{\text{qubit}} = \exp \left[\sum_{ph} \frac{it_h^p}{2} (X_p Y_h - Y_p X_h) \right], \quad (13)$$

$$\approx \prod_{ph} \exp \left[\frac{it_h^p}{2} (X_p Y_h - Y_p X_h) \right], \quad (14)$$

where the last expression corresponds to a first-order Trotter approximation with a single step, which we adopt in this work. Each terms in Eq. (14) can be implemented

as a Givens rotation gate acting on qubits p and h :

$$G(2\theta) = \begin{pmatrix} 1 & 0 & 0 & 0 \\ 0 & \cos \theta & -\sin \theta & 0 \\ 0 & \sin \theta & \cos \theta & 0 \\ 0 & 0 & 0 & 1 \end{pmatrix}. \quad (15)$$

Thus, the pUCCD ansatz can be implemented as a sequence of Givens rotations on top of a reference state, e.g., initially prepared by applying X gates to the qubits corresponding to occupied pair orbitals. Fig. 2 illustrates two circuit layouts for preparing the pUCCD ansatz, taking ^{22}O nucleus as an example. (a) pUCCD(GS): optimized for devices with limited connectivity (e.g., IBM heavy-hexagon architectures), using Givens rotations followed by SWAP gates (GS) [21]. The basic idea behind the circuit is detailed in Ref. [36]. (b) pUCCD(G): one realization for all-to-all connectivity (e.g., trapped-ion devices) using only Givens rotations (G). In both cases, the number of parameters, angles of Givens rotations, is the same, given by the number of particle-hole pairs.

However, the circuit depth and number of two-qubit gates slightly differ. While pUCCD(GS) has a nearly unique circuit layout, pUCCD(G) admits many realizations depending on the choice of initial configuration and ordering of Givens rotations. We will therefore present simulator results for pUCCD(G) as distributions over multiple circuit realizations in Sec. III. In what follows, we use a single deterministic realization for both pUCCD(GS) and pUCCD(G) unless otherwise noted.

As a related study, it should be noted that a work by Sarma et al. [15] considered oxygen isotopes in the sd shell on a trapped-ion quantum computer, IonQ Aria, using a variant of unitary coupled cluster doubles (UCCD) ansatz. Their UCCD ansatz was applied only to time-reversal nucleon pairs (denoted $\text{UCCD}(\nu = 0)$ in the following where ν is the seniority). Although formally equivalent to DOCI, their implementation yielded ground-state errors of 3 – 13% relative to FCI, depending on the isotope. One limitation arises from the scaling of circuit parameters: the number of Givens rotations to express the excitations/de-excitations of nucleon pairs grows rapidly with system size, making direct application to heavier isotopes impractical.

By contrast, the pUCCD ansatz with a single Trotter step scales more favorably, as

$$N_{\text{param}} = N_{\text{occ.}}(N_q - N_{\text{occ.}}), \quad (16)$$

where $N_{\text{occ.}}$ is the number of occupied pairs and N_q the number of qubits in the HCB representation. This scaling is significantly milder than that of $\text{UCCD}(\nu = 0)$, as summarized in Table II. Note that the FCI dimension is also shown in the table for reference, and these show the number of configurations in the so-called M-scheme, i.e. the basis states are labeled by the sum of the j_z values of the single-particle states. For even number of neutrons, all the states with different total angular momentum J are included in the $M = 0$ subspace leading to the FCI dimension shown in the table.

TABLE II. Dimension and number of parameters in ansatz. Comparison of FCI dimension and the number of parameters in the circuits for $\text{UCCD}(\nu = 0)$ [15] and pUCCD ansatz. The $\text{UCCD}(\nu = 0)$ is unitary coupled cluster doubles ansatz where the configurations are restricted to zero-seniority configurations. The rightmost column means the pair unitary coupled cluster doubles ansatz with a single Trotter step.

Nucleus	FCI (M=0)	UCCD($\nu = 0$)	pUCCD
$^{18}\text{O}, ^{26}\text{O}$	14	5	5
$^{20}\text{O}, ^{24}\text{O}$	81	14	8
^{22}O	142	19	9
$^{42}\text{Ca}, ^{58}\text{Ca}$	30	9	9
$^{44}\text{Ca}, ^{56}\text{Ca}$	565	44	16
$^{46}\text{Ca}, ^{54}\text{Ca}$	3,952	119	21
$^{48}\text{Ca}, ^{52}\text{Ca}$	12,022	209	24
^{50}Ca	17,276	251	25
$^{58}\text{Ni}, ^{76}\text{Ni}$	19	10	10
$^{60}\text{Ni}, ^{74}\text{Ni}$	365	54	18
$^{62}\text{Ni}, ^{72}\text{Ni}$	3,103	164	24
$^{64}\text{Ni}, ^{70}\text{Ni}$	12,240	329	28
$^{66}\text{Ni}, ^{68}\text{Ni}$	23,884	461	30

C. Measurement of energy expectation values

Once the ansatz circuit is prepared, the next task is to evaluate the expectation value of the Hamiltonian. First, we discuss our optimization approach; then we detail the measurement strategies. In this work, the parameters of the pUCCD ansatz were optimized on statevector simulators using the Adam optimizer with PennyLane [37]. This is still an idealized setting, but good starting point to evaluate the ansatz quality and measurement strategies, and to benchmark hardware results. The strategy to optimize the ansatz circuit on a real device is left as a future issue. Optimization directly on quantum hardware remains an open problem, for which gradient-free sequential approaches [38] may offer a promising path.

Once the ansatz circuit is prepared, the next task is to evaluate the expectation value of the Hamiltonian. For noise-free simulations, one does not need to care about the measurement strategy, but it is crucial point to be considered for noisy simulations and experiments on hardware.

Diagonal terms in the computational basis, i.e., operators involving $\{I, Z_i, Z_i \otimes Z_j\}$, can be obtained by measuring the ansatz circuit in the computational basis. In this case, post-selection techniques is naturally applicable: bitstrings violating the particle number of the target system are discarded.

In contrast, non-diagonal terms $\{X_i \otimes X_j, Y_i \otimes Y_j\}$ require additional circuits. Both XX and YY terms are local, i.e., free from Z -strings, and contribute equally to the energy expectation value. Thus, all $X_p X_q$ terms can be evaluated by a single additional circuit, ansatz followed by Hadamard gates on all qubits prior to measurement, and $\langle Y_p Y_q \rangle$ terms can be evaluated by doubling the $\langle X_p X_q \rangle$ results. This approach will be referred

to as the *Hadamard* method in the following. While straightforward, this method does not preserve particle-number symmetry, limiting the use of post-selection. The other approach employed in this work is one to be referred to as *Basis rotations*, which involves diagonalizing $XX + YY$ terms in the computational basis prior to measurement [21, 39]:

$$\begin{aligned} \langle \psi | X_p X_q + Y_p Y_q | \psi \rangle \\ = \langle \psi | \mathcal{U}_{p,q}(\pi/4)(Z_p - Z_q)\mathcal{U}_{p,q}^\dagger(\pi/4) | \psi \rangle, \end{aligned} \quad (17)$$

where $\mathcal{U}_{p,q}(\theta)$ can be implemented as a Givens rotation $G(2\theta)$ on qubits p and q . In accordance with the discussion in Ref. [39], the required terms can be grouped such that only $2\lfloor N_q/2 \rfloor$ additional circuits are needed to measure all the $XX + YY$ terms, where N_q is the number of qubits. Importantly, this strategy preserves particle-number symmetry, enabling effective post-selection.

Note that since we measure diagonal and off-diagonal contributions in separate circuits, the summed estimate of the energy is not strictly variational even after post-selection. However, in practice, we observed that the energy estimates distributed around the noise-free values from statevector simulations, hence non-variational nature does not pose significant issues in this work.

D. Implementation of Givens rotation gates

To construct the pUCCD ansatz circuits (Fig. 2) and to perform basis rotations for diagonalizing the $XX + YY$ terms, it is necessary to implement Givens rotation gates. Several approaches are known in literature and we examined the following three methods:

1. Magic-gate method (Ref. [40]) - implements Givens rotation using a sequence of "magic" gates.
2. $\sqrt{\text{SWAP}}$ -based method (Ref. [36]) - uses $\sqrt{\text{SWAP}}$ gates to construct the Givens rotation.
3. Controlled- R_y method (Ref. [41]) - equivalent to a breakdown of controlled- R_y followed by CNOT gates.

At the raw circuit level, these methods require 2, 4, and 3 CNOT gates per Givens rotation, respectively. However, we found the number of corresponding 2-qubit native gates for the transpiled/compiled circuits are equivalent to each other. As a result, the total number of the 2-qubit gates for pUCCD(GS) and pUCCD(G) ansatze scales as $3N_G$ and $2N_G$, respectively. Here, N_G is the number of Givens rotations. Thus, the choice of the implementation method can be made based on convenience and the first method was adopted in this work.

Quantum circuits submitted to the hardware are transformed to native gate sets of the adopted hardware. On the RIKEN-Quantinuum's Reimei device, two-qubit native gates are ZZPhase gates, $\exp(-i\pi\alpha/2(Z_p \otimes Z_q))$.

Here we follow the notation of pytket [42], i.e., angle parameter is given in the unit of $\pi/2$. In practice, the compiled circuit uses exactly twice as many ZZPhase gates as there are Givens rotations.

E. Hardware information

We now describe the quantum hardware used in this work. The Reimei is based on Quantinuum's H-1 series trapped-ion quantum computer, and has 20 qubits with all-to-all connectivity. The Reimei device was installed in RIKEN's Wako campus, and started its operation in February 2025. Table III summarizes the calibration data of the Reimei device, which were measured on 2025-05-09. The reported metrics include single- and two-qubit gate errors, SPAM (state preparation and measurement) errors, crosstalk, and memory error rates. These parameters provide a baseline for evaluating the quality of quantum circuits executed on the device. In particular, the relatively low one- and two-qubit gate error rates, combined with the all-to-all connectivity of trapped-ion hardware, enable the accurate implementation of the pUCCD ansatz circuits described in this work.

The experiments on the Reimei trapped-ion quantum computer of this work were carried out via the Quantinuum Nexus [43] platform, which enables users to run quantum simulations on various backends, including noise-free statevector simulators, emulators, and real devices.

TABLE III. Calibration data of the Reimei device. The values are from data on 2025-05-09 via the Quantinuum's Nexus [43] platform.

Error type	Value	Uncertainty
One-qubit gate error P_1	4.22×10^{-5}	5.23×10^{-6}
Two-qubit gate error P_2	1.39×10^{-3}	5.92×10^{-5}
SPAM error (0)	2.73×10^{-3}	1.57×10^{-4}
SPAM error (1)	5.25×10^{-3}	2.18×10^{-4}
Crosstalk error	3.21×10^{-5}	1.89×10^{-6}
Memory error	2.83×10^{-4}	2.32×10^{-5}

III. RESULTS

In this section, we present the results of the pUCCD ansatz both on noise-free statevector simulators and on the Reimei quantum hardware for the ground-state energies of oxygen, calcium, and nickel isotopes. The former allows us to assess the intrinsic accuracy of the pUCCD ansatz, while the latter demonstrates the feasibility of executing the pUCCD ansatz on real quantum hardware.

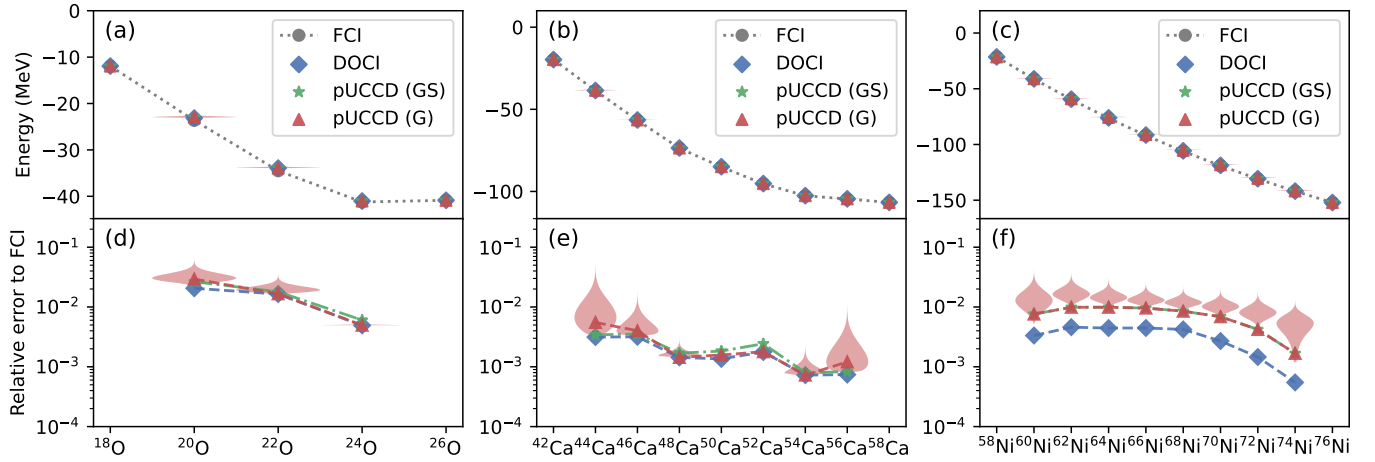


FIG. 3. Ground-state energies of target isotopes on noise-free statevector simulators. (a)–(c) Ground-state energies of oxygen, calcium, and nickel isotopes, respectively. Full configuration interaction (FCI, dotted lines with gray circles) and doubly occupied configuration interaction (DOCI, blue diamonds) are compared with statevector simulations using the pUCCD(GS) ansatz (green stars) and the pUCCD(G) ansatz (red triangles). Here, pUCCD(GS) denotes the pUCCD ansatz implemented with nearest-neighbor Givens rotations and SWAP gates, while pUCCD(G) assumes all-to-all connectivity, as realized in the Reimei device. (d)–(f) Differences between the pUCCD ansatz results and the DOCI results are shown relative to FCI in logarithmic scale. Uncertainty bands for pUCCD(G) are obtained by random sampling over circuits with different initial configurations and Givens-rotation orderings.

A. Ideal simulation results of the pUCCD ansatz

We first assess the performance of the pUCCD ansatz on a noiseless statevector simulator, thereby probing its intrinsic accuracy in approximating ground-state energies of the target isotopes. Full Configuration Interaction (FCI) provides the exact ground-state energies within the valence space, serving as a benchmark for evaluating the accuracy of approximate methods. Doubly Occupied Configuration Interaction (DOCI) is another approximate method that restricts the configuration space to zero-seniority configurations, i.e., states in which all nucleons are paired as time-reversed partners. In noise-free simulations, any deviation from FCI obtained with the pUCCD ansatz reflects intrinsic limitations of the ansatz itself, independent of hardware noise or statistical noise due to the finite number of measurement shots.

In what follows, we consider two types of pUCCD ansatz, named pUCCD(GS) and pUCCD(G). The (GS) represents Givens plus SWAP, which consists of only nearest neighbor Givens rotations and thereby more suitable for hardware with a limited connectivity [21, 39]. On the other hand, (G) stands for Givens rotations where all-to-all connectivity is assumed. In experiments on the Reimei device, we will focus on the pUCCD(G) ansatz.

Fig. 3 shows ground-state energies for the target isotopes, obtained with pUCCD(G) and pUCCD(GS) on noise-free statevector simulators compared to FCI and DOCI results. The upper panels (a)–(c) display the ground-state energies. At this scale, all curves are nearly indistinguishable. The lower panels (d)–(f) show the differences between pUCCD and DOCI results relative to

FCI in logarithmic scale. Results for two-neutron (or two-neutron-hole) systems are omitted in the lower panels, since both DOCI and pUCCD exactly reproduce FCI in those cases.

For the pUCCD ansatz, the symbols show the results of one representative realization of the ansatz, and the uncertainty bands are plotted for the pUCCD(G) ansatz. We generated many pUCCD(G) realizations by varying the initial configuration and the order of Givens rotations in the ansatz circuit. The resulting energies from a skewed distribution around the representative realization, and the uncertainty bands are constructed by fitting Gamma distributions to the histograms of sampled energies. More technical details are provided in the Supplemental Material [33].

Most importantly, pUCCD reproduces DOCI energies with an error of mostly less than 1%, while using far fewer parameters, demonstrating its compact yet accurate description. For reference, DOCI itself reproduces FCI ground-state energies within 0.1 – 1%, with deviations smaller than the typical uncertainties (a few percent) of modern nuclear many-body methods [44]. The residual differences depend on the target system: Ca isotopes in the pf shell are well described within the zero-seniority space, whereas oxygen isotopes show larger contributions from higher-seniority configurations leading to slightly larger deviations from FCI. Nickel isotopes in the $jj45$ shell exhibit larger discrepancies between DOCI and pUCCD compared to oxygen and calcium isotopes. This arises from the factors intrinsic to the $jj45$ shell. The valence space, $jj45$ shell, consists of four jj -coupling orbitals ($1p_{1/2}, 1p_{3/2}, 0f_{5/2}, 0g_{9/2}$), and the configuration

TABLE IV. Summary of pUCCD results on the RIKEN-Quantinuum Reimei device. FCI and ideal pUCCD are classical results. Reimei columns report hardware energies using Hadamard or basis-rotation measurements; errors are relative to ideal pUCCD. Valid ratio is the fraction of bitstrings passing particle-number post-selection.

Nuclide	FCI	Ideal pUCCD	Reimei: Hadamard		Reimei: Basis rotation		Valid ratio (%)
	Energy (MeV)	Energy (MeV)	Energy (MeV)	Rel. Error (%)	Energy (MeV)	Rel. Error (%)	
¹⁸ O	-11.932	-11.932	-11.802	1.09	-11.893	0.33	98
²⁰ O	-23.632	-22.939	-22.383	2.42	-22.854	0.37	98
²² O	-34.498	-33.924	-33.560	1.07	-33.829	0.28	97
²⁴ O	-41.225	-41.021	-40.985	0.09	-41.027	0.02	97
²⁶ O	-40.869	-40.869	-40.613	0.63	-40.940	0.18	96
⁴² Ca	-19.734	-19.734	-19.727	0.04	-19.775	0.21	97
⁴⁴ Ca	-38.675	-38.462	-38.540	0.20	-38.424	0.10	97
⁴⁶ Ca	-56.667	-56.440	-56.414	0.05	-56.565	0.22	96
⁴⁸ Ca	-73.662	-73.556	-73.538	0.02	-73.489	0.09	95
⁵⁰ Ca	-85.055	-84.921	-85.135	0.25	-85.007	0.10	94
⁵² Ca	-95.360	-95.190	-95.038	0.16	-95.149	0.04	94
⁵⁴ Ca	-102.632	-102.557	-102.622	0.06	-102.648	0.09	94
⁵⁶ Ca	-104.589	-104.462	-104.620	0.15	-104.325	0.13	94
⁵⁸ Ca	-106.666	-106.666	-106.885	0.20	-106.668	<0.01	94
⁵⁸ Ni	-21.447	-21.447	-21.207	1.12	-21.291	0.73	93
⁶⁰ Ni	-41.276	-40.961	-40.752	0.51	-40.992	0.07	94
⁶² Ni	-59.602	-59.013	-58.703	0.52	-59.015	<0.01	93
⁶⁴ Ni	-76.444	-75.687	-76.027	0.45	-75.765	0.10	92
⁶⁶ Ni	-91.941	-91.059	-90.552	0.56	-90.695	0.40	93
⁶⁸ Ni	-106.140	-105.237	-105.169	0.06	-105.288	0.05	92
⁷⁰ Ni	-119.034	-118.215	-118.189	0.02	-118.158	0.05	91
⁷² Ni	-130.930	-130.379	-130.511	0.10	-130.397	0.01	95
⁷⁴ Ni	-141.932	-141.694	-141.565	0.09	-141.715	0.02	93
⁷⁶ Ni	-152.103	-152.103	-151.986	0.08	-152.054	0.03	94

mixing among these orbitals is pronounced in Ni isotopes even for ground states since their effective single particle energies are close to each other [28]. The single-Trotter pUCCD ansatz, while efficient for capturing pairing correlations, becomes less expressive in the presence of such strong configuration mixing.

B. Results on RIKEN-Quantinuum's Reimei trapped-ion quantum device

We now report the hardware results for ground-state energies of oxygen, calcium, and nickel isotopes using the pUCCD(G) ansatz on Reimei. Table IV summarizes exact FCI energies, the ideal pUCCD results from noise-free statevector simulations, and the experimentally measured energies with two measurement strategies along with percent errors relative to the ideal pUCCD results and valid ratios. The valid ratio indicates the ratio of bitstrings that preserve the correct particle number of the target nucleus after measurement, reflecting the hardware fidelity in preparing the desired state. The numbers are from ansatz measurements, hence independent of the measurement strategy for $XX + YY$ terms.

As a whole, the hardware results agree closely with the noise-free simulations, showing relative errors mostly below 0.3% to the ideal pUCCD results, and at most a few percent relative to FCI. These results demonstrate

the capability of current quantum hardware to accurately capture nuclear pairing correlations.

This trend is further supported by bootstrapping analyses. Fig. 4 displays the relative errors of ground-state energies obtained on Reimei for oxygen, calcium, and nickel isotopes, using both measurement strategies. Error bars represent 1σ statistical uncertainties evaluated by bootstrapping with 500 resamplings of datasets obtained from 1,024 measurement shots. The shaded band corresponds to a 0.3% error for reference. Most data points fall within this range.

Note again that the difference between Hadamard and Basis rotation methods lies only in the measurement of $XX + YY$ terms, while diagonal terms are measured in the same way for both methods. Between the two measurement strategies, the basis-rotation method consistently outperforms the Hadamard method, yielding results closer to ideal simulations. Lighter isotopes exhibit larger uncertainties because $XX + YY$ terms contribute to the total energy relatively larger in lighter isotopes. In contrast, for heavier isotopes, the mass-dependent scaling commonly applied to two-body matrix elements in phenomenological shell-model interactions reduces the absolute size of the $XX + YY$ contributions (e.g., TBMEs for ⁵⁸Ca and ⁷⁸Ni are multiplied by ~ 0.9 compared with ⁴²Ca and ⁵⁸Ni), which further diminishes their relative contribution to the total energy.

Next, we further examine the statistical uncertain-

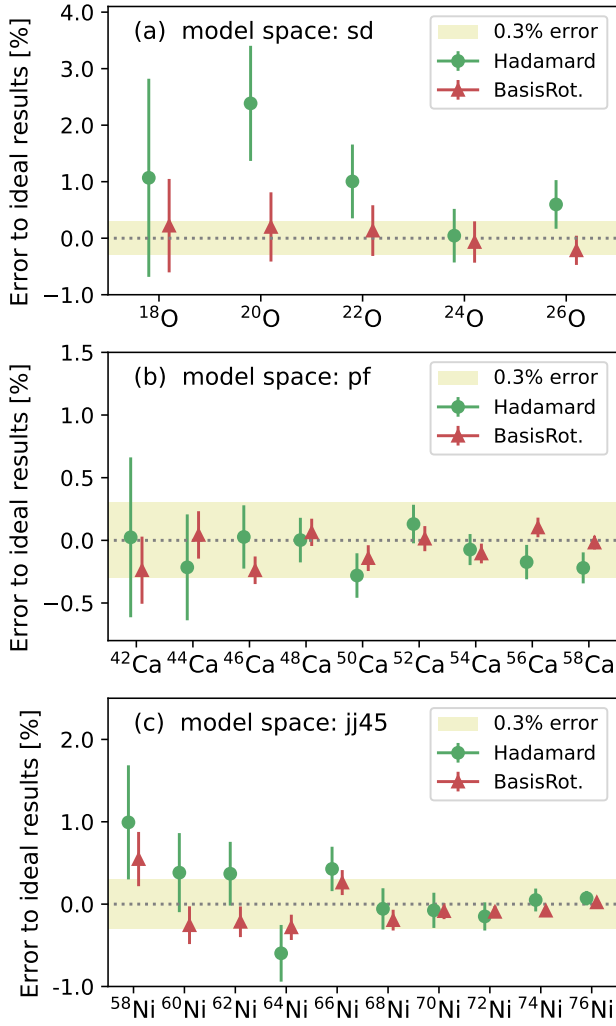


FIG. 4. Relative errors in ground-state energies on the RIKEN-Quantinuum Reimei device. The results are shown for oxygen (a), calcium (b), and nickel (c) isotopes, using two measurement strategies: Hadamard and basis rotation. The error bars represent 1σ statistical uncertainties evaluated by bootstrapping, and the shaded band corresponds to a 0.3% error.

ties by separating the total energy into diagonal and $XX+YY$ contributions. As an illustration, Fig. 5, shows the distribution of the ground-state energy of ^{66}Ni obtained by resampling the data 500 times. The energy is separated into contributions from diagonal terms (top panel) and $XX+YY$ terms (bottom panel). Vertical dashed lines indicate the corresponding noise-free statevector results for comparison.

The accuracy on the diagonal term depends primarily on occupation numbers, while the $XX+YY$ terms are contribution is more sensitive to both occupation numbers and relative phases between configurations. As shown in the lower panel of Fig. 5, the distribution obtained using the Hadamard method is noticeably broader than that obtained with basis rotations.

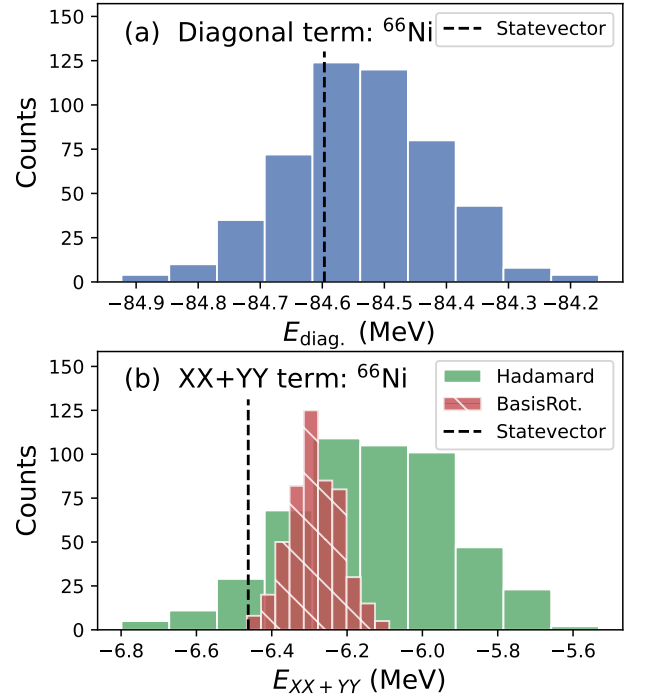


FIG. 5. Bootstrapping of hardware results for ^{66}Ni . (a) diagonal terms. (b) $XX+YY$ terms evaluated by two measurement strategies: Hadamard (green) and basis rotation (red with hatching). The vertical dashed line shows the ideal statevector simulation result. The bin width is automatically determined by the Freedman-Diaconis rule.

We emphasize, however, that this analysis does not account for systematic errors inherent to the Reimei device. Therefore, our results do not imply that the basis-rotation method always outperforms the Hadamard method in practice. Nonetheless, the observed trends (see also Fig. 4) suggest that basis rotations tend to yield more stable estimates of energy expectation values for the systems studied here.

IV. SUMMARY AND OUTLOOK

Quantum many-body systems have become a central focus of quantum computing research over the past decade, driven by rapid progress in algorithms and hardware. However, demonstrating genuine quantum advantage in interacting many-body physics remains an open challenge, requiring advances in all components of the algorithmic workflow: ansatz design, quantum algorithms, measurement strategies, optimization techniques, and so on. This work concentrated on the ansatz and measurement aspects, from the standpoint of nuclear structure, where exceptionally strong correlations make the choice of ansatz especially critical.

By combining a hard-core boson mapping of the nuclear shell-model Hamiltonian with a pair-unitary coupled cluster doubles (pUCCD) ansatz, we demonstrated

accurate ground-state calculations of oxygen, calcium, and nickel isotopes on the RIKEN-Quantinuum Reimei trapped-ion quantum computer. Our results achieve sub-percent agreement with noise-free statevector simulations, setting a new benchmark for nuclear-structure simulations on real NISQ hardware.

Although the pUCCD parameters were optimized using classical simulators, this proof-of-principle study highlights how physically motivated, compact ansätze can deliver accurate results with modest qubit numbers and circuit depths. Such strategies may guide the discovery of efficient variational forms for larger systems where classical pre-optimization is infeasible.

Looking ahead, incorporating proton-neutron interactions will require ansätze capable of describing more general non-local correlations beyond pairing. Nonetheless, the present results demonstrate the viability of pUCCD for multi-neutron (or multi-proton) systems, and point toward applications to heavier systems such as neutron drops or neutron-rich isotopes. As an illustration of possible extensions, entropy-driven entanglement forging [45] has recently been proposed to localize correlations in Adapt-VQE circuits; similar ideas could be combined with pUCCD, for instance by monitoring generalized seniority. In addition, hybrid qubit encoding schemes [46] could be extended to nuclear systems.

Beyond ansatz design, new algorithmic paradigms merit exploration. Quantum subspace diagonalization techniques [47–51], including Quantum Krylov and related methods, use quantum devices to generate subspace states while delegating diagonalization to classical post-processing. These approaches provide access to ex-

cited states and transition properties such as electromagnetic transitions. Such hybrid methods, in combination with physically motivated ansätze and developing efficient schemes for time evolution and measurement, may offer a promising path toward realistic quantum simulations of nuclear systems beyond the reach of classical methods.

DATA AVAILABILITY STATEMENT

The data presented in this manuscript, including circuits and encoded Hamiltonians, are available from the GitHub repository and the Zenodo archive [52]. For classical calculations, the exact diagonalization results can be reproduced by using the NuclearToolkit.jl package [25] with the interaction files available through KSHELL [24]. We utilized the Qiskit [53], PennyLane [37], and pytket [42] for quantum computations. Experiments on the Reimei device were carried out using the Quantinuum’s Nexus [43] platform.

ACKNOWLEDGMENTS

This research was supported in part by JSPS Grant-in-Aid for Scientific Research (Grant Nos. JP22K14030, JP25H01511, JP25K01688), JST PRESTO (Grant No. JPMJPR25F8), JST COI-NEXT (Grant No. JPMJPF2221), MEXT Q-LEAP (Grant No. JPMXS0118067246), and RIKEN TRIP initiative (Nuclear Transmutation). This work is based on the results obtained from a project, JPNP20017, commissioned by the New Energy and Industrial Technology Development Organization (NEDO).

-
- [1] N. Yoshioka, T. Okubo, Y. Suzuki, Y. Koizumi, and W. Mizukami, Hunting for quantum-classical crossover in condensed matter problems, *npj Quantum Information* **10**, 45 (2024).
 - [2] A. Peruzzo, J. McClean, P. Shadbolt, M.-H. Yung, X.-Q. Zhou, P. J. Love, A. Aspuru-Guzik, and J. L. O’Brien, A variational eigenvalue solver on a photonic quantum processor, *Nat. Commun.* **5**, 4213 (2014).
 - [3] K. Bharti, A. Cervera-Lierta, T. H. Kyaw, T. Haug, S. Alperin-Lea, A. Anand, M. Degroote, H. Heimonen, J. S. Kottmann, T. Menke, W.-K. Mok, S. Sim, L.-C. Kwek, and A. Aspuru-Guzik, Noisy intermediate-scale quantum algorithms, *Rev. Mod. Phys.* **94**, 015004 (2022).
 - [4] M. Larocca, S. Thanasilp, S. Wang, K. Sharma, J. Biamonte, P. J. Coles, L. Cincio, J. R. McClean, Z. Holmes, and M. Cerezo, Barren plateaus in variational quantum computing, *Nature Reviews Physics* **7**, 174 (2025).
 - [5] A. Katabarwa, K. Gratsea, A. Caesura, and P. D. Johnson, Early fault-tolerant quantum computing, *PRX Quantum* **5**, 020101 (2024).
 - [6] S.-J. Ran, Encoding of matrix product states into quantum circuits of one- and two-qubit gates, *Phys. Rev. A* **101**, 032310 (2020).
 - [7] T. Felser, S. Notarnicola, and S. Montangero, Efficient tensor network ansatz for high-dimensional quantum many-body problems, *Phys. Rev. Lett.* **126**, 170603 (2021).
 - [8] D. Malz, G. Styliaris, Z.-Y. Wei, and J. I. Cirac, Preparation of matrix product states with log-depth quantum circuits, *Phys. Rev. Lett.* **132**, 040404 (2024).
 - [9] E. F. Dumitrescu, A. J. McCaskey, G. Hagen, G. R. Jansen, T. D. Morris, T. Papenbrock, R. C. Pooser, D. J. Dean, and P. Lougovski, Cloud quantum computing of an atomic nucleus, *Phys. Rev. Lett.* **120**, 210501 (2018).
 - [10] D. Lacroix, Symmetry-assisted preparation of entangled many-body states on a quantum computer, *Phys. Rev. Lett.* **125**, 230502 (2020).
 - [11] A. Pérez-Obiol, A. M. Romero, J. Menéndez, A. Rios, A. García-Sáez, and B. Juliá-Díaz, Nuclear shell-model simulation in digital quantum computers, *Sci. Rep.* **13**, 12291 (2023).
 - [12] J. E. García-Ramos, A. Sáiz, J. M. Arias, L. Lamata, and P. Pérez-Fernández, Nuclear physics in the era of quantum computing and quantum machine learning, *Advanced Quantum Technologies* **n/a**, 2300219 (2023).

- [13] Savage, Martin J., Quantum computing for nuclear physics, *EPJ Web Conf.* **296**, 01025 (2024).
- [14] O. Kiss, M. Grossi, P. Lougovski, F. Sanchez, S. Vallecorsa, and T. Papenbrock, Quantum computing of the ${}^6\text{Li}$ nucleus via ordered unitary coupled clusters, *Phys. Rev. C* **106**, 034325 (2022).
- [15] C. Sarma, O. Di Matteo, A. Abhishek, and P. C. Srivastava, Prediction of the neutron drip line in oxygen isotopes using quantum computation, *Phys. Rev. C* **108**, 064305 (2023).
- [16] H. R. Grimsley, S. E. Economou, E. Barnes, and N. J. Mayhall, An adaptive variational algorithm for exact molecular simulations on a quantum computer, *Nature Communications* **10**, 3007 (2019).
- [17] T. Otsuka, T. Suzuki, R. Fujimoto, H. Grawe, and Y. Akaishi, Evolution of nuclear shells due to the tensor force, *Phys. Rev. Lett.* **95**, 232502 (2005).
- [18] K. Hebeler, Three-nucleon forces: Implementation and applications to atomic nuclei and dense matter, *Physics Reports* **890**, 1 (2021), three-nucleon forces: Implementation and applications to atomic nuclei and dense matter.
- [19] C. Gu, Z. H. Sun, G. Hagen, and T. Papenbrock, Entanglement entropy of nuclear systems, *Phys. Rev. C* **108**, 054309 (2023).
- [20] S. Yoshida, T. Sato, T. Ogata, T. Naito, and M. Kimura, Accurate and precise quantum computation of valence two-neutron systems, *Phys. Rev. C* **109**, 064305 (2024).
- [21] V. E. Elfving, M. Millaruelo, J. A. Gámez, and C. Gogolin, Simulating quantum chemistry in the seniority-zero space on qubit-based quantum computers, *Phys. Rev. A* **103**, 032605 (2021).
- [22] T. E. O'Brien, G. Anselmetti, F. Gkritis, V. E. Elfving, S. Polla, W. J. Huggins, O. Oumarou, K. Kechedzhi, D. Abanin, R. Acharya, I. Aleiner, R. Allen, T. I. Andersen, K. Anderson, M. Ansmann, F. Arute, K. Arya, A. Asfaw, J. Atalaya, J. C. Bardin, A. Bengtsson, G. Bortoli, A. Bourassa, J. Bovaird, L. Brill, M. Broughton, B. Buckley, D. A. Buell, T. Burger, B. Burkett, N. Bushnell, J. Campero, Z. Chen, B. Chiaro, D. Chik, J. Cogan, R. Collins, P. Conner, W. Courtney, A. L. Crook, B. Curtin, D. M. Debroy, S. Demura, I. Drozdov, A. Dunsworth, C. Erickson, L. Faoro, E. Farhi, R. Fatemi, V. S. Ferreira, L. Flores Burgos, E. Forati, A. G. Fowler, B. Foxen, W. Giang, C. Gidney, D. Gilboa, M. Giustina, R. Gosula, A. Grajales Dau, J. A. Gross, S. Habegger, M. C. Hamilton, M. Hansen, M. P. Harrigan, S. D. Harrington, P. Heu, M. R. Hoffmann, S. Hong, T. Huang, A. Huff, L. B. Ioffe, S. V. Isakov, J. Iveland, E. Jeffrey, Z. Jiang, C. Jones, P. Juhas, D. Kafri, T. Khattar, M. Khezri, M. Kieferová, S. Kim, P. V. Klimov, A. R. Klots, A. N. Korotkov, F. Kostritsa, J. M. Kreikebaum, D. Landhuis, P. Laptev, K. M. Lau, L. Laws, J. Lee, K. Lee, B. J. Lester, A. T. Lill, W. Liu, W. P. Livingston, A. Locharla, F. D. Malone, S. Mandrà, O. Martin, S. Martin, J. R. McClean, T. McCourt, M. McEwen, X. Mi, A. Mieszala, K. C. Miao, M. Mohseni, S. Montazeri, A. Morvan, R. Movassagh, W. Mruczkiewicz, O. Naaman, M. Neeley, C. Neill, A. Nersisyan, M. Newman, J. H. Ng, A. Nguyen, M. Nguyen, M. Y. Niu, S. Omonije, A. Opremcak, A. Petukhov, R. Potter, L. P. Pryadko, C. Quintana, C. Rocque, P. Roushan, N. Saei, D. Sank, K. Sankaragomathi, K. J. Satzinger, H. F. Schurkus, C. Schuster, M. J. Shearn, A. Shorter, N. Shutty, V. Shvarts, J. Skrzynny, W. C. Smith, R. D. Somma, G. Sterling, D. Strain, M. Szalay, D. Thor, A. Torres, G. Vidal, B. Villalonga, C. Vollgraf, Heidweiller, T. White, B. W. K. Woo, C. Xing, Z. J. Yao, P. Yeh, J. Yoo, G. Young, A. Zalcman, Y. Zhang, N. Zhu, N. Zobrist, D. Bacon, S. Boixo, Y. Chen, J. Hilton, J. Kelly, E. Lucero, A. Megrant, H. Neven, V. Smelyanskiy, C. Gogolin, R. Babbush, and N. C. Rubin, Purification-based quantum error mitigation of pair-correlated electron simulations, *Nature Physics* **19**, 1787 (2023).
- [23] L. Zhao, J. Goings, K. Shin, W. Kyoung, J. I. Fuks, J.-K. Kevin Rhee, Y. M. Rhee, K. Wright, J. Nguyen, J. Kim, and S. Johri, Orbital-optimized pair-correlated electron simulations on trapped-ion quantum computers, *npj Quantum Information* **9**, 60 (2023).
- [24] N. Shimizu, Nuclear shell-model code for massive parallel computation, "KSHELL" (2013), [arXiv:1310.5431](https://arxiv.org/abs/1310.5431); N. Shimizu, T. Mizusaki, Y. Utsuno, and Y. Tsunoda, Thick-restart block Lanczos method for large-scale shell-model calculations, *Comput. Phys. Commun.* **244**, 372 (2019).
- [25] S. Yoshida, NuclearToolkit.jl: A Julia package for nuclear structure calculations, *Journal of Open Source Software* **7**, 4694 (2022); <https://github.com/SotaYoshida/NuclearToolkit.jl>.
- [26] B. A. Brown and W. A. Richter, New "USD" Hamiltonians for the sd shell, *Phys. Rev. C* **74**, 034315 (2006).
- [27] M. Honma, T. Otsuka, B. A. Brown, and T. Mizusaki, Shell-model description of neutron-rich pf-shell nuclei with a new effective interaction GXPF 1, *Eur. Phys. J. A* **25**, 499 (2005).
- [28] M. Honma, T. Otsuka, T. Mizusaki, and M. Hjorth-Jensen, New effective interaction for $f_5p_{g_9}$ -shell nuclei, *Phys. Rev. C* **80**, 064323 (2009).
- [29] A. Volya, B. Brown, and V. Zelevinsky, Exact solution of the nuclear pairing problem, *Physics Letters B* **509**, 37 (2001).
- [30] T. M. Henderson, G. E. Scuseria, J. Dukelsky, A. Signoracci, and T. Duguet, Quasiparticle coupled cluster theory for pairing interactions, *Phys. Rev. C* **89**, 054305 (2014).
- [31] T. M. Henderson, I. W. Bulik, and G. E. Scuseria, Pair extended coupled cluster doubles, *The Journal of Chemical Physics* **142**, 214116 (2015).
- [32] Y. Qiu, T. M. Henderson, T. Duguet, and G. E. Scuseria, Particle-number projected bogoliubov-coupled-cluster theory: Application to the pairing hamiltonian, *Phys. Rev. C* **99**, 044301 (2019).
- [33] Supplementary material for this work: url will be provided.
- [34] Y. S. Yordanov, D. R. M. Arvidsson-Shukur, and C. H. W. Barnes, Efficient quantum circuits for quantum computational chemistry, *Phys. Rev. A* **102**, 062612 (2020).
- [35] Y. S. Yordanov, V. Armaos, C. H. W. Barnes, and D. R. M. Arvidsson-Shukur, Qubit-excitation-based adaptive variational quantum eigensolver, *Communications Physics* **4**, 228 (2021).
- [36] I. D. Kivlichan, J. McClean, N. Wiebe, C. Gidney, A. Aspuru-Guzik, G. K.-L. Chan, and R. Babbush, Quantum simulation of electronic structure with linear depth and connectivity, *Phys. Rev. Lett.* **120**, 110501 (2018).

- [37] V. Bergholm, J. Izaac, M. Schuld, C. Gogolin, S. Ahmed, V. Ajith, M. S. Alam, G. Alonso-Linaje, B. Akash-Narayanan, A. Asadi, J. M. Arrazola, U. Azad, S. Banning, C. Blank, T. R. Bromley, B. A. Cordier, J. Ceroni, A. Delgado, O. D. Matteo, A. Dusko, T. Garg, D. Guala, A. Hayes, R. Hill, A. Ijaz, T. Isacsson, D. Ittah, S. Jahangiri, P. Jain, E. Jiang, A. Khandelwal, K. Kottmann, R. A. Lang, C. Lee, T. Loke, A. Lowe, K. McKiernan, J. J. Meyer, J. A. Montañez-Barrera, R. Moyard, Z. Niu, L. J. O’Riordan, S. Oud, A. Panigrahi, C.-Y. Park, D. Polatajko, N. Quesada, C. Roberts, N. Sá, I. Schoch, B. Shi, S. Shu, S. Sim, A. Singh, I. Strandberg, J. Soni, A. Száva, S. Thabet, R. A. Vargas-Hernández, T. Vincent, N. Vitucci, M. Weber, D. Wierichs, R. Wiersema, M. Willmann, V. Wong, S. Zhang, and N. Killoran, [Pennylane: Automatic differentiation of hybrid quantum-classical computations](#) (2022), [arXiv:1811.04968 \[quant-ph\]](#).
- [38] K. M. Nakanishi, K. Fujii, and S. Todo, Sequential minimal optimization for quantum-classical hybrid algorithms, [Phys. Rev. Res.](#) **2**, 043158 (2020).
- [39] G. A. Quantum and Collaborators, Hartree-fock on a superconducting qubit quantum computer, [Science](#) **369**, 1084 (2020).
- [40] F. Vatan and C. Williams, Optimal quantum circuits for general two-qubit gates, [Phys. Rev. A](#) **69**, 032315 (2004).
- [41] J. M. Arrazola, O. Di Matteo, N. Quesada, S. Jahangiri, A. Delgado, and N. Killoran, Universal quantum circuits for quantum chemistry, [Quantum](#) **6**, 742 (2022).
- [42] S. Sivarajah, S. Dilkes, A. Cowtan, W. Simmons, A. Edgington, and R. Duncan, $t|ket\rangle$: a retargetable compiler for nisd devices, [Quantum Science and Technology](#) **6**, 014003 (2020); [pytket-quantinuum](#).
- [43] [Quantinuum nexus](#) (2024).
- [44] H. Hergert, A guided tour of ab initio nuclear many-body theory, [Frontiers in Physics](#) **8**, 379 (2020).
- [45] A. Pérez-Obiol, S. Masot-Llima, A. M. Romero, J. Menéndez, A. Ríos, A. García-Sáez, and B. Juliá-Díaz, [Entropy-driven entanglement forging](#) (2024), [arXiv:2409.04510 \[quant-ph\]](#).
- [46] F. J. del Arco Santos and J. S. Kottmann, A hybrid qubit encoding: splitting fock space into fermionic and bosonic subspaces, [Quantum Science and Technology](#) **10**, 035018 (2025).
- [47] N. H. Stair, R. Huang, and F. A. Evangelista, A multireference quantum krylov algorithm for strongly correlated electrons, [Journal of Chemical Theory and Computation](#) **16**, 2236 (2020).
- [48] C. L. Cortes and S. K. Gray, Quantum krylov subspace algorithms for ground- and excited-state energy estimation, [Phys. Rev. A](#) **105**, 022417 (2022).
- [49] K. Kanno, M. Kohda, R. Imai, S. Koh, K. Mitarai, W. Mizukami, and Y. O. Nakagawa, [Quantum-selected configuration interaction: classical diagonalization of hamiltonians in subspaces selected by quantum computers](#) (2023), [arXiv:2302.11320 \[quant-ph\]](#).
- [50] J. Robledo-Moreno, M. Motta, H. Haas, A. Javadi-Abhari, P. Jurcevic, W. Kirby, S. Martiel, K. Sharma, S. Sharma, T. Shirakawa, I. Sitdikov, R.-Y. Sun, K. J. Sung, M. Takita, M. C. Tran, S. Yunoki, and A. Mezzacapo, Chemistry beyond the scale of exact diagonalization on a quantum-centric supercomputer, [Science Advances](#) **11**, eadu9991 (2025).
- [51] N. Yoshioka, M. Amico, W. Kirby, P. Jurcevic, A. Dutt, B. Fuller, S. Garion, H. Haas, I. Hamamura, A. Ivrii, R. Majumdar, Z. Mineev, M. Motta, B. Pokharel, P. Rivero, K. Sharma, C. J. Wood, A. Javadi-Abhari, and A. Mezzacapo, Krylov diagonalization of large many-body hamiltonians on a quantum processor, [Nature Communications](#) **16**, 5014 (2025).
- [52] S. Yoshida, [Reimei_pUCCD_ShellModel v1.0](#) (2025).
- [53] Qiskit contributors, [Qiskit: An open-source framework for quantum computing](#) (2023).

SUPPLEMENTAL MATERIAL

In this Supplemental Material, we provide supplementary information regarding (i) the derivation of the hard-core-boson form of the nuclear Hamiltonian, (ii) the uncertainty bands of the pUCCD(G) ansatz, (iii) the results of the pUCCD(GS) ansatz on IBM's noisy simulator, and (iv) description of Zenodo archive containing data analyzed in this work.

V. DERIVATION OF HARD-CORE-BOSON FORM OF THE HAMILTONIAN

Here we present the detailed derivation of the pair-wise Hamiltonians for the systems of interest, corresponding to Eq. (2) of the main text. Starting from the fermionic Hamiltonian with up to two-body interactions, we introduced time-reversal pairs (i, \bar{i}) and defined pair creation, annihilation, and number operators in Eqs. (4)–(5).

After reorganizing terms and discarding those irrelevant within the zero-seniority space, the Hamiltonian reduces to the following forms:

$$\sum_i \varepsilon_i a_i^\dagger a_i = \sum_{i < 0} (\varepsilon_i a_i^\dagger a_i + \varepsilon_{\bar{i}} a_{\bar{i}}^\dagger a_{\bar{i}}) = \sum_{\tilde{i}} \varepsilon_{\tilde{i}} N_{\tilde{i}}, \quad (18)$$

$$\frac{1}{4} \sum_{ijkl} V_{ijkl} a_i^\dagger a_j^\dagger a_k a_l = \frac{1}{4} \sum_{ij} V_{i\bar{i}j\bar{j}} a_i^\dagger a_{\bar{i}}^\dagger a_j a_{\bar{j}} + \frac{1}{4} \sum_{i,j \notin \{i,\bar{i}\}} V_{ijij} a_i^\dagger a_j^\dagger a_j a_i + (\text{irrelevant terms}), \quad (19)$$

$$\frac{1}{4} \sum_{i,j \in \{i,\bar{i}\}} V_{i\bar{i}j\bar{j}} a_i^\dagger a_{\bar{i}}^\dagger a_j a_{\bar{j}} = \frac{1}{4} \left(\sum_i V_{i\bar{i}i\bar{i}} a_i^\dagger a_{\bar{i}}^\dagger a_i a_{\bar{i}} + \sum_i V_{i\bar{i}i\bar{i}} a_i^\dagger a_{\bar{i}}^\dagger a_i a_{\bar{i}} \right) = \frac{1}{2} \sum_i V_{i\bar{i}i\bar{i}} a_i^\dagger a_{\bar{i}}^\dagger a_i a_{\bar{i}} = \sum_{i < 0} V_{i\bar{i}i\bar{i}} a_i^\dagger a_{\bar{i}}^\dagger a_i a_{\bar{i}}, \quad (20)$$

$$\frac{1}{4} \sum_{i,j \notin \{i,\bar{i}\}} V_{i\bar{i}j\bar{j}} a_i^\dagger a_{\bar{i}}^\dagger a_j a_{\bar{j}} = \sum_{i < 0} \sum_{j \notin \{i,\bar{i}\} < 0} V_{i\bar{i}j\bar{j}} a_i^\dagger a_{\bar{i}}^\dagger a_j a_{\bar{j}} = \sum_{i \neq j < 0} V_{i\bar{i}j\bar{j}} a_i^\dagger a_{\bar{i}}^\dagger a_j a_{\bar{j}}, \quad (21)$$

$$\frac{1}{4} \sum_{i,j \notin \{i,\bar{i}\}} V_{ijij} a_i^\dagger a_j^\dagger a_j a_i = \frac{1}{4} \sum_{i,j \notin \{i,\bar{i}\}} V_{ijij} n_i n_j \quad (22)$$

where the indices i, j, k, l denote a Fermionic single-particle states having $\{n, l, j, j_z, t_z\}$ quanta. The \tilde{i}, \tilde{j} represent pair-wise basis states obtained by folding single-particle states i and \bar{i} (the time-reversed partner). Rewriting these in terms of pair operators defined in Eqs. (3)–(5) of the main text, we obtain

$$\sum_{i < 0} V_{i\bar{i}i\bar{i}} a_i^\dagger a_{\bar{i}}^\dagger a_i a_{\bar{i}} \rightarrow \sum_{\tilde{i}} V_{\tilde{i}\tilde{i}}^p A_{\tilde{i}}^\dagger A_{\tilde{i}}, \quad (23)$$

$$\sum_{i \neq j < 0} V_{i\bar{i}j\bar{j}} a_i^\dagger a_{\bar{i}}^\dagger a_j a_{\bar{j}} \rightarrow \sum_{\tilde{i} \neq \tilde{j}} V_{\tilde{i}\tilde{j}}^p A_{\tilde{i}}^\dagger A_{\tilde{j}}, \quad (24)$$

$$\frac{1}{4} \sum_{i,j \notin \{i,\bar{i}\}} V_{ijij} n_i n_j \rightarrow \sum_{\tilde{i} \neq \tilde{j}} V_{\tilde{i}\tilde{j}}^m N_{\tilde{i}} N_{\tilde{j}}, \quad (25)$$

where we put the superscripts p and m to distinguish pairing and monopole terms, respectively.

VI. UNCERTAINTY BANDS OF THE PUCCD(G) ANSATZ

The pUCCD(G) ansatz can be realized in many different circuit layouts due to all-to-all connectivity. The number of possible circuits grows combinatorially with system size (e.g. for ^{50}Ca , 252 possible reference states and 25! permutations of Givens rotations). Exhaustive sampling is thus impractical.

To estimate uncertainties, we generated 1,000 random circuits per nucleus, varying both the initial occupied qubits and the ordering of Givens rotations. The resulting energy distributions (examples shown in Fig. 6 for ^{20}O , ^{50}Ca , and ^{66}Ni) are asymmetric but well approximated by a Gamma distribution. To ensure physical plausibility, the lower bound of the distribution was set to the lowest energy encountered in the samples, thereby avoiding unphysical assignment of energies below DOCI.

The fitted Gamma distributions were then used to construct the shaded uncertainty bands in Fig. (3) of the main text. We note that the pUCCD(GS) ansatz typically yields results close to the optimal edge of the pUCCD(G)

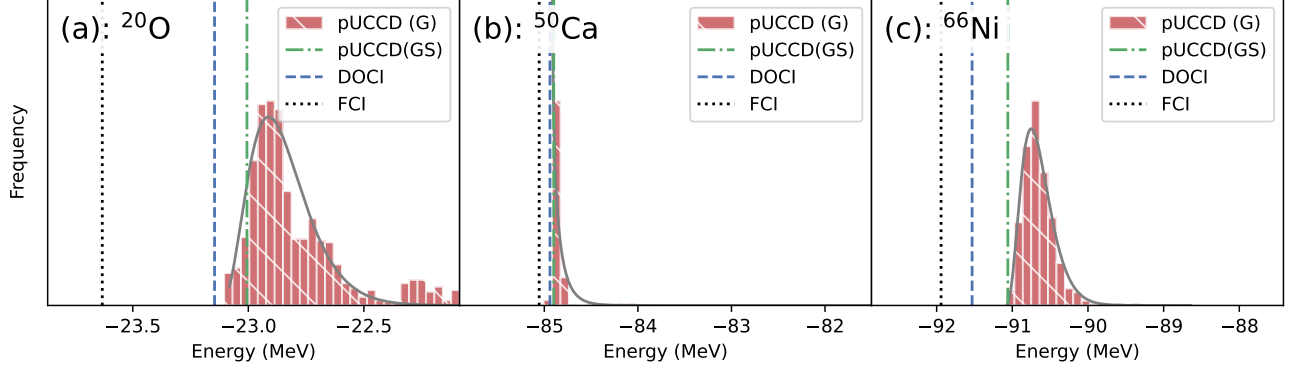


FIG. 6. Uncertainty estimation for pUCCD(G) results. Sampled possible realization of ansatz is fitted by a Gamma distribution for the pUCCD results of (a) ^{20}O , (b) ^{50}Ca and (c) ^{66}Ni .

distribution, except for cases such as ^{24}O , ^{50}Ca , and ^{52}Ca where the qubit ordering or single-particle energy structure leads to less favorable initialization.

VII. RESULTS OF THE PUCCD(GS) ANSATZ ON IBM'S NOISY SIMULATOR

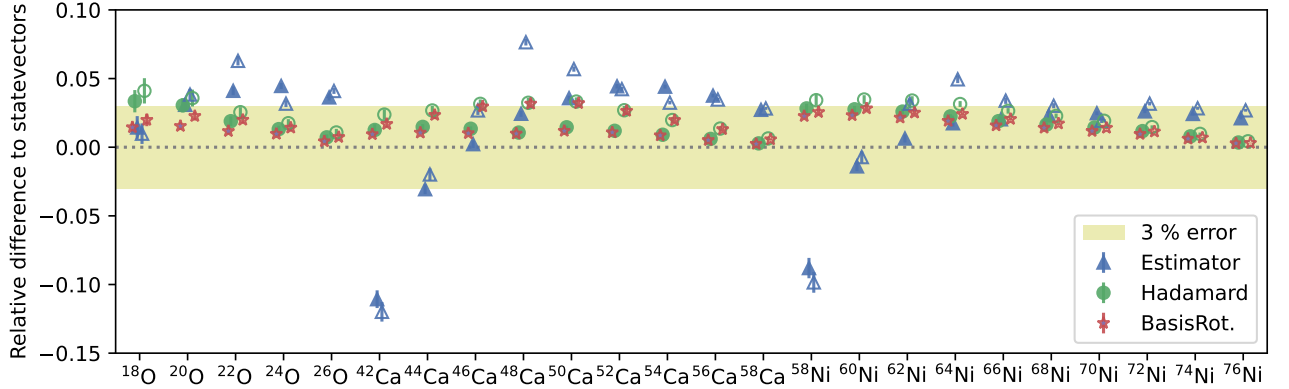


FIG. 7. pUCCD results on IBM's noisy simulator. Relative error to the ideal statevector simulation for the pUCCD ansatz. Closed markers correspond to Givens+SWAP (GS) circuits, open markers to Givens-only (G) circuits. Colors and markers indicate different measurement strategies as explained in the text. The shaded band denotes 3% deviation from the statevector results. Error bars show the standard deviation of 100 independent runs.

For completeness, we benchmark the pUCCD(GS) ansatz on IBM's noisy simulator (FakeTorino backend), which reflects the heavy-hexagon connectivity of IBM devices. In this setting, additional SWAP gates are required, increasing the number of two-qubit gates to $3N_G$ (where N_G is the number of Givens rotations), compared to $2N_G$ under all-to-all connectivity. Figure 7 summarizes the relative errors with respect to the ideal statevector simulations. Three measurement strategies were compared:

- **Estimator** (blue triangles): direct expectation-value evaluation.
- **Hadamard method** (green circles): Hadamard gates are applied to access XX terms, with YY inferred by symmetry.
- **Basis-rotation method** (red stars): $XX + YY$ terms are diagonalized via Givens rotations, enabling particle-number post-selection.

While all approaches yield errors within a few percent, the basis-rotation strategy consistently provides more stable results. In lighter nuclei, we observe a tendency to overestimate the binding energy with Estimator results. This

behavior can be traced back to the measurement outcomes: bit strings corresponding to states with an incorrect particle number may occasionally appear. When such spurious configurations correspond to nuclei with a larger number of valence particles, they often yield lower expectation values of the Hamiltonian, i.e. artificial more bindings. As a result, the statistical averaging over these bit strings leads to an overbinding bias in light isotopes, where the relative contribution of such erroneous configurations is more pronounced.

VIII. DESCRIPTION OF DATA ARCHIVE

The data that support the findings of this study are openly available in:

- Zenodo at <https://doi.org/10.5281/zenodo.8314085>
- GitHub repository at https://github.com/SotaYoshida/Reimei_pUCCD_ShellModel.

One can find the following data in the repository and archive:

- `circuit_parameters`: Optimized parameters for pUCCD ansatze.
- `Data_measured`: measured data on IBM's FakeTorino simulator and random sampling data for uncertainty estimation.
- `interaction_file`: interaction files used in this work.
- `pytket_circuits`: pytket circuit files for pUCCD ansatze.
- `qiskit_Hamiltonians`: encoded Hamiltonians in qiskit format.
- `retrieved_data`: measurement results retrieved from the Reimei quantum computer for both emulator and real hardware runs.